RESEARCH PAPER

HYDROTHERMAL MEDIATED $FeWO_4$/rGO COMPOSITE FOR SUPERIORITY AT REMOVAL OF FLUORIDE AND BACTERIA FROM CONTAMINATED WATER

B N SURESH VARMA[1,2], P. SHYAMALA[1*], B. LEELA KUMARI[3], G ANUSHA[4]

[1]Department of Chemistry, Andhra University, Visakhapatnam, 530003, India
[2]Shri Vishnu Engineering College for Women (A), Bhimavaram, Andhra Pradesh, 534202, India
[3]Department of Chemistry, Chaitanya Degree College for Women, Gajuwaka, Visakhapatnam, Andhra Pradesh, 530026, India
[4]Department of Engineering Physics, SRKR Engineering College, Chinaamiram, Bhimavaram, Andhra Pradesh, 534204, India

Correspondence email: dr.pshyamala@andhrauniversity.edu.in

ABSTRACT

The development of efficient and sustainable material for fluoride removal from contaminated water remains a critical environmental challenge. In this study, iron tungstate ($FeWO_4$) and $FeWO_4$/reduced graphene oxide (rGO) nanocomposite were synthesized via hydrothermal approach and systematically evaluated for defluorination performance. Structural and surface characteristics were examined using X-Ray diffraction analysis (XRD), Scanning electron microscopy (SEM), Energy dispersive X-ray spectroscopy (EDS), BET Surface analyzer, X-Ray photoelectron spectroscopy (XPS), Ultraviolet Visible spectroscopy, Thermogravimetric analysis (TGA) and Fourier Transform Infrared spectroscopy (FTIR). The results confirmed the formation of monoclinic $FeWO_4$ with average crystallite sizes of 21.3 nm $FeWO_4$ and 16.9 nm for $FeWO_4$/rGO composite, indicating effective dispersion of $FeWO_4$ on GO sheets. The incorporation of rGO slightly reduced the band gap (eV) from 2.71 to 2.21 for $FeWO_4$ and $FeWO_4$/rGO respectively. The $FeWO_4$/rGO nanocomposite exhibited higher fluoride removal efficiency (33%) than pristine $FeWO_4$ (21%). Maximum adsorption efficiency of 44% was achieved at 25 mg dosage, with optimal removal at low fluoride concentration (58% at 2 mg L^{-1}). Adsorption was favored at 30°C indicating exothermic behavior. The composite also showed good reusability and retained its crystalline structure after five cycles. The antibacterial performance of $FeWO_4$ and $FeWO_4$/rGO nanocomposites was investigated against the Gram-positive bacterium S. aureus and the Gram-negative bacterium E. coli using the agar diffusion technique. For S. aureus, $FeWO_4$ showed inhibition zones of 14, 17 and 19 mm at 100, 50 and 10 µg/mL, respectively, whereas $FeWO_4$/rGO exhibited higher activity with inhibition zones of 22 and 20 mm at 100 and 50 µg/mL respectively. For E. coli, $FeWO_4$ demonstrated inhibition zones of 12, 16 and 19 mm, while $FeWO_4$/rGO showed limited activity with a maximum inhibition zone of 10 mm at 100 µg/mL. The enhanced antibacterial activity of $FeWO_4$/rGO against S. aureus may be attributed to the synergistic effect of rGO promoting reactive oxygen species generation and membrane disruption. These results indicate that $FeWO_4$ is more effective against E. coli, whereas $FeWO_4$/rGO exhibits superior activity against S. aureus at higher concentrations.

Keywords: $FeWO_4$/rGO, Hydrothermal approach, Fluoride removal, anti-bacterial activity.

How to cite this article: Varma BNS, Shyamala P, Leela Kumari B, Anusha G. Hydrothermal Mediated $FeWO_4$/rGO Composite for Superiority at Removal of Fluoride and Bacteria from Contaminated Water. Int J Drug Deliv Technol. 2026;16(54s): 962-972. DOI: 10.25258/ijddt.16.54s.84

Source of support: Nil.
Conflict of interest: None.

1. Introduction

Iron tungstate ($FeWO_4$), a transition metal tungstate with a monoclinic wolframite crystal structure, has gained significant interest owing to its excellent chemical stability, narrow band gap and desirable redox characteristics[1,2]. Owing to the presence of Fe^{2+}/Fe^{3+} and W^{6+} ions, $FeWO_4$ exhibits unique electronic and catalytic characteristics that make it a promising candidate for applications in photocatalysis, adsorption, electrochemical energy storage, and environmental remediation[3–5]. In particular, $FeWO_4$ has demonstrated notable potential in the removal of inorganic and organic contaminants from water, including fluoride ions and dye pollutants, due to its strong surface affinity and chemical robustness[6,7]. However, the practical performance of pristine $FeWO_4$ is often limited by factors such as low surface area, particle agglomeration, and rapid recombination of photogenerated charge carriers[8].

To overcome these limitations, hybridization of $FeWO_4$ with carbon-based nanomaterials has emerged as an effective strategy. Among various carbon-based materials, reduced graphene oxide (rGO) is extensively recognized for its large surface area, superior electrical conductivity, and excellent mechanical stability[9,10]. The incorporation of rGO into metal oxide systems can significantly enhance charge transport, suppress electron–hole

recombination, and improve adsorption capacity by providing abundant active sites and π–π interactions[11,12]. Consequently, $FeWO_4$/rGO nanocomposites have been developed to exploit the synergistic interaction between the metal tungstate and the graphene matrix[13].

Recent studies have reported that $FeWO_4$/rGO nanocomposites exhibit superior performance compared to pristine $FeWO_4$ in photocatalytic dye degradation, antibacterial activity, and adsorption-based water purification processes[14–16]. The rGO sheets not only act as conductive pathways for efficient electron transfer but also facilitate uniform dispersion of $FeWO_4$ nanoparticles, thereby enhancing structural stability and functional efficiency[17,18]. These advantages make $FeWO_4$/rGO nanocomposites attractive multifunctional materials for sustainable environmental applications. Therefore, systematic investigation of the synthesis, structural properties, and functional performance of $FeWO_4$/rGO composites is essential to further advance their application in water treatment technologies. In this study the $FeWO_4$/rGO nanocomposites were synthesized by the hydrothermal method a sustainable approach that removed the fluoride ion and shown its enhanced antibacterial activity. This method provides several benefits, including operational simplicity, low cost, eco-friendly nature, non-toxicity, reproducibility and effective control over nanoparticle formation.

2. Experimental section

2.1. Materials used

Graphite, Ferric nitrate ($Fe(NO_3)_2$), Sodium tungstate (Na_2WO_4), Sodium hydroxide (NaOH), Sodium borohydride($NaBH_4$), Sodium nitrate ($NaNO_3$), Potassium permanganate ($KMnO_4$), Hydrogen peroxide (H_2O_2), and Sulphuric acid (H_2SO_4) were procured from Merck India with analytical reagent (AR) grade purity (>98%). Double-distilled water (2D) was used throughout the experimental work.

2.2. Synthesis of $FeWO_4$/rGO composite

The hydrothermal method was used to create the $FeWO_4$/rGO composite. First, 50 milliliters of double distilled water was mixed with equal amounts of $Fe(NO_3)_2$ and Na_2WO_4, and the mixture was stirred for one hour. Following the stirring process, the pre-calculated GO (50 mg) was incorporated into the mixture solution and permitted to stir for an additional hour. The homogeneous mixture solution was transferred to a Teflon beaker, which was then placed inside a stainless-steel hydrothermal bomb. This setup was sealed and maintained in a hot air stabilizer, where it underwent heating at 180 ºC for 5 hours. The device should be allowed to cool to room temperature after completing the procedure. The product was then isolated from the solution through repeated centrifugation and washing with water, followed by drying in an oven overnight at 60ºC. The identical method was employed to synthesize $FeWO_4$ in the absence of GO. Graphene oxide (GO) was synthesized using the modified Hummers' method[27].

2.3. Characterization

The crystallite size and phase composition of the synthesized materials were analyzed using a powder X-ray diffractometer (Bruker D8) equipped with Cu–Kα radiation ((\lambda = 1.54) Å), operated at 30 kV and 40 mA. The optical properties and band gap energies were determined using a UV–Visible spectrophotometer (Shimadzu 2600R), with $BaSO_4$ used as the reference material. X-ray photoelectron spectroscopy (XPS) analysis was carried out using a Shimadzu instrument with an Al–Kα radiation source (1489.5 eV), operated at an emission current of 10 mA and voltage of 15 kV to investigate the electronic states of the synthesized nanomaterials. The morphology and elemental composition of the $FeWO_4$/rGO composite were examined by transmission electron microscopy (TEM) coupled with energy-dispersive X-ray analysis (EDX) using a JEM-2100 instrument operated at 200 kV. Samples were prepared on carbon-coated copper grids for imaging. Functional groups present in the synthesized materials were identified using Fourier transform infrared spectroscopy (FTIR, Bruker ALPHA-E) in the range of 900–4000 cm^{-1} with a resolution of 4 cm^{-1}. The specific surface area of the synthesized samples was measured using a Nova 2200e BET surface area analyzer under liquid nitrogen conditions.

2.4. Fluoride removal experiment

The fluoride ion removal efficiency of $FeWO_4$ and $FeWO_4$/rGO nanocomposites was calculated using the following equation (Eq.1)where (C_0) represents the initial fluoride concentration and (C_t) represents the fluoride concentration after adsorption at time (t). The $FeWO_4$/rGO nanocomposite exhibited higher fluoride removal efficiency (33%) compared to pristine $FeWO_4$ (21%), indicating the enhanced adsorption capability of the rGO-incorporated composite.

$$\text{Removal } \% = \frac{C_o - C_t}{C_o} \times 100 \qquad \text{Eq. 1}$$

Here, C_o and C_t are the absorbance of the collected solution at time 'zero' and 't' respectively.

2.5. Antimicrobial performance

The antimicrobial potential of the samples was determined using the agar well diffusion technique as described by Perez et al. (1990). Sterile cotton swabs were used to evenly distribute microbial inoculum across the surface of the solidified Müller–Hinton agar plates. Wells were then aseptically punched into the agar and aliquots of the test samples (100 µg/mL, 50 µg/mL, and 10 µg/mL prepared from a 1 mg/mL stock solution) were introduced into the respective wells. Plates inoculated with *E. coli* and *A. niger* were incubated at 37°C for 24 hours. Following incubation, the

antimicrobial activity was evaluated by measuring the diameter (mm) of the inhibition zones formed around each well.

3. Results and discussion

3.1.X-Ray Diffraction (XRD) analysis

Figure 1 illustrates the XRD patterns of GO, $FeWO_4$, and the $FeWO_4$/rGO nanocomposite recorded in the 2θ range of 10–90°. The diffraction pattern of GO exhibits a broad peak centered at approximately 2θ =11°, corresponding to the (001) plane[4], which arises from increased interlayer spacing due to the presence of oxygen-containing functional groups, confirming the successful oxidation of graphite to graphene oxide. The XRD pattern of $FeWO_4$ displays a series of sharp and well-defined diffraction peaks at 2θ ≈ 23.5°, 30.2°, 35.6°, 40.4°, 49.8°, 54.3°, 60.8°, 65.2°, and 72.4°, which can be indexed to the (100), (011), (111), (020), (121), (211), (031), (220), and (221) crystallographic planes, respectively. These diffraction peaks are consistent with the standard JCPDS card No. 21-0863, confirming the successful formation of monoclinic wolframite-structured $FeWO_4$ with good crystallinity and phase purity[19].

In the $FeWO_4$/rGO nanocomposite, all characteristic diffraction peaks of $FeWO_4$ are retained, indicating that the crystal structure of $FeWO_4$ remains unchanged after integration with rGO. Notably, the disappearance of the GO (001) peak at 10–11° in the composite pattern suggests effective reduction of GO to rGO and exfoliation of graphene layers during composite synthesis. The slight reduction in peak intensity and minor broadening observed in the composite may be attributed to strong interfacial interactions between $FeWO_4$ nanoparticles and rGO sheets, as well as improved dispersion of $FeWO_4$ within the graphene matrix. These results collectively confirm the successful synthesis of the $FeWO_4$/rGO nanocomposite. The average crystalline size(D) of hydrothermally prepared material was measured by Deby-Scherer formula Eqn (2) and the average crystalline size of the $FeWO_4$ is obtained as 14.58nm and the $FeWO_4$/rGO nanocomposite is calculated and found to be 6.6nm.

3.2. FTIR analysis

Figure 2 shows the FTIR spectra of pristine $FeWO_4$ and the $FeWO_4$/rGO nanocomposite recorded in the range of 4000–500 cm^{-1}. The spectrum of $FeWO_4$ exhibits characteristic absorption bands associated with the metal–oxygen framework of iron tungstate. The strong absorption band observed below 700 cm^{-1}, with a prominent peak near 570 cm^{-1}, is attributed to the stretching vibrations of Fe–O and W–O bonds in the wolframite crystal structure, confirming the formation of $FeWO_4$. A weak and broad band in the region of 3300cm^{-1} can be ascribed to O–H stretching vibrations arising from surface-adsorbed water molecules or hydroxyl groups. The absorption feature around 2350 cm^{-1} is commonly associated with atmospheric CO_2 and does not originate from the sample itself[20]. In the FTIR spectrum of the $FeWO_4$/rGO nanocomposite, several notable changes are observed. The intensity of the broad O–H stretching band in the 3300 cm^{-1} region is reduced compared to pristine $FeWO_4$, indicating partial reduction of oxygen-containing functional groups during composite formation. Additionally, weak bands in the region of 1650 cm^{-1} correspond to the skeletal vibration of sp^2-bonded C=C in reduced graphene oxide, confirming the presence of rGO in the composite. The characteristic Fe–O and W–O vibration bands below 700 cm^{-1} remain clearly visible in the composite spectrum, demonstrating that the $FeWO_4$ crystal structure is preserved after integration with rGO. The strong interfacial interaction between $FeWO_4$ nanoparticles and rGO sheets is expected to facilitate charge transfer and enhance the functional efficiency of the composite for photocatalytic and environmental applications.

3.3. Scanning electron microscopy

The surface morphology of the synthesized $FeWO_4$ and $FeWO_4$/RGO nanocomposites were investigated using SEM, as illustrated in Fig. 3(a–d). The low-magnification image (Fig. 3a) reveals the characteristic wrinkled and sheet-like architecture, indicating the effective incorporation of $FeWO_4$ nanoparticles onto its surface. At higher magnification (Fig. 3b), the $FeWO_4$ nanoparticles exhibit predominantly spherical to polyhedral shapes and are homogeneously dispersed across the graphene layers. The intermediate magnification image (Fig. 3c) further demonstrates the formation of a dense and uniform coating of $FeWO_4$ nanoparticles on the RGO sheets, which helps prevent restacking of graphene layers while increasing the available surface area[21]. The figure 3d confirms that the $FeWO_4$ nanoparticles are firmly anchored onto the conductive RGO matrix, with particle sizes mainly ranging from 20–50 nm, along with occasional larger agglomerates measuring approximately 60–80 nm. This well-integrated nanostructure, consisting of uniformly distributed $FeWO_4$ nanoparticles on RGO nanosheets, is expected to provide enhanced surface area, improved electrical conductivity, and better structural stability, making it highly suitable for electrochemical applications.

3.4. Energy Dispersive X-Ray Spectroscopy (EDS)

A comparative evaluation of the EDS results for pristine $FeWO_4$ and $FeWO_4$/rGO nanocomposite provides valuable insight into the compositional changes induced by rGO incorporation. In the case of $FeWO_4$, the EDS spectrum confirms the presence of Oxygen (O), Iron (Fe), and Tungsten (W) as the principal elements, with oxygen contributing 40.88 wt% (71.30 at%), iron 56.73 wt% (28.34 at%), and tungsten 2.39 wt% (0.36 at%) were shown in figure

4. This elemental distribution is consistent with the stoichiometry of iron tungstate and confirms the successful formation of a pure $FeWO_4$ phase without detectable impurities[22].

In contrast, the EDS analysis of the $FeWO_4$/rGO nanocomposite reveals the additional presence of carbon (C) alongside O, Fe, and W, confirming the successful integration of reduced graphene oxide into the composite matrix. In this case, oxygen accounts for 41.24 wt% (65.52 at%), iron for 51.44 wt% (23.36 at%), tungsten for 2.09 wt% (0.29 at%), and carbon for 5.13 wt% (10.83 at%). The slight decrease in the relative weight and atomic percentages of iron and tungsten in the composite, compared to pristine $FeWO_4$, can be attributed to the incorporation of carbon from rGO, which modifies the overall elemental composition.

The comparatively low atomic percentage of tungsten observed in both samples is primarily due to its high atomic mass, resulting in a smaller atomic fraction despite a measurable weight contribution. Importantly, the appearance of carbon in the $FeWO_4$/rGO sample, coupled with the retention of Fe and W signals, confirms that rGO incorporation does not disrupt the iron tungstate framework but instead forms a hybrid nanocomposite through effective interfacial integration.

3.5. Transmission electron microscopy

The transmission electron microscopy (TEM) images presented in Fig.5(a–f) provide detailed insight into the morphology and microstructural features of the synthesized $FeWO_4$/rGO nanocomposite. At low magnification (Fig.5a), the sample exhibits irregularly shaped agglomerates, indicating the clustering of nanoparticles within the graphene framework. Fig.5(b) reveals that these aggregates are composed of densely packed nanograins, suggesting strong interparticle interactions.

The selected area electron diffraction (SAED) pattern shown in Fig. 5(c) exhibits concentric diffraction rings, indicating the polycrystalline nature of $FeWO_4$. These rings correspond to different crystallographic planes, confirming its crystalline structure[23]. In contrast, the TEM image in Fig. 5(d) reveals nearly spherical to slightly irregular nanoparticles with a broad size distribution, suggesting partial agglomeration during the synthesis process.

A more detailed view in Fig.5(e) shows that the individual nanoparticles vary in size, with larger particles surrounded by smaller ones, forming a heterogeneous nanostructure. This variation in particle size can contribute to increased surface area and enhanced reactivity. Furthermore, the SAED pattern in Fig.5(f) exhibits distinct bright spots along with diffuse rings, indicating the coexistence of crystalline $FeWO_4$ and the partially disordered structure of reduced graphene oxide (rGO).

3.6. BET Surface area and Porosity Analysis

Nitrogen adsorption–desorption measurements were carried out to evaluate the surface characteristics and porosity of the prepared material. The analysis was performed using N_2 as the adsorptive at 77 K under standard BET conditions. The sample mass used for the measurement was 0.07 g. The adsorption–desorption isotherm reveals distinct features indicative of the material's pore structure. At very low relative pressures ($P/P_0 < 0.05$), a sharp increase in nitrogen uptake is observed, which is characteristic of strong adsorbate–surface interactions and suggests the presence of microporous domains. This initial steep region corresponds to monolayer adsorption and is critical for determining the BET surface area. As the relative pressure increases, the adsorption curve gradually transitions into a multilayer adsorption regime, showing a steady but moderate increase in adsorbed volume.

Furthermore, the isotherm displays a noticeable hysteresis loop in the intermediate to high relative pressure range (P/P_0=0.4–1.0), which is typically associated with capillary condensation within mesoporous structures[24]. According to IUPAC classification, this behavior corresponds to a Type IV isotherm confirming the coexistence of mesoporosity along with limited microporosity. The relatively narrow hysteresis loop suggests a uniform pore size distribution and well-defined pore channels.

The maximum nitrogen adsorption capacity reaches approximately 35 $cm^3\ g^{-1}$ for $FeWO_4$ and 38 $cm^3\ g^{-1}$ for $FeWO_4$/rGO at P/P_0 close to unity, indicating a moderate specific surface area compared to highly porous nanomaterials. In contrast, the second isotherm shows a significantly higher adsorption volume 120$cm^3\ g^{-1}$, reflecting a much larger surface area and a predominantly microporous nature with minimal hysteresis. This suggests that structural modification, possibly through incorporation of carbonaceous components such as reduced graphene oxide, enhances surface accessibility and adsorption capacity. The observed adsorption behavior confirms that the material possesses a hierarchical pore structure, combining both micro and mesoporous features.

3.7. Thermogravimetric analysis

Figure 7 presents the thermogravimetric (TGA) profiles of pristine $FeWO_4$ and the $FeWO_4$/rGO nanocomposite recorded from room temperature to 1000°C. The TGA curve of $FeWO_4$ demonstrates high thermal stability, with a minimal weight loss of approximately 2% throughout the temperature range. The slight mass loss below 150°C is mainly attributed to the removal of physically adsorbed moisture and weakly bound surface species[25]. A gradual and negligible weight reduction between 200 and 600°C may be associated with the removal of residual hydroxyl groups and minor structural changes within the $FeWO_4$ lattice. Beyond 600°C,

the curve remains nearly constant, confirming the high thermal robustness and structural stability of $FeWO_4$.

In contrast, the $FeWO_4$/rGO nanocomposite exhibits a more noticeable weight loss due to the incorporation of reduced graphene oxide. The initial slight mass loss below 150°C is attributed to the removal of physically adsorbed water. A gradual weight reduction up to 400°C is associated with the decomposition of residual oxygen containing functional groups on the rGO sheets. A major weight loss observed between 400 and 600°C is mainly related to the thermal decomposition of the carbonaceous rGO component, which is associated with the thermal decomposition and partial oxidation of the rGO carbon framework. After 600°C, the mass of the composite stabilizes, indicating that the remaining material consists predominantly of thermally stable $FeWO_4$.

The total weight loss of the $FeWO_4$/rGO nanocomposite is estimated to be around 7–8%, which corresponds to the carbonaceous content contributed by rGO. The comparison of both curves demonstrates that while $FeWO_4$ exhibits superior intrinsic thermal stability, the $FeWO_4$/rGO composite maintains adequate stability up to high temperatures, making it suitable for photocatalytic and environmental applications. Furthermore, the intimate interaction between $FeWO_4$ nanoparticles and rGO sheets likely enhances the thermal endurance of the composite by restricting rapid carbon degradation.

3.8. UV-Visible spectroscopy

Figure 8 shows the UV–visible absorption spectra of pristine $FeWO_4$ and the $FeWO_4$/rGO nanocomposite in the wavelength range of 200–800 nm. Both materials exhibit broad absorption in the UV and visible regions, suggesting their suitability as visible-light-responsive materials.

The $FeWO_4$ sample shows a gradual increase in absorbance from the UV region toward the visible range, followed by a sharp absorption edge around 580 nm, which is characteristic of iron tungstate[26]. This absorption behavior can be attributed to electronic transitions from the valence band, primarily composed of O 2p orbitals, to the conduction band formed by Fe 3d and W 5d states. The absorption edge position confirms the semiconducting nature of $FeWO_4$ and its capability to absorb visible light.

In comparison, the $FeWO_4$/rGO nanocomposite exhibits slightly enhanced absorption intensity throughout the visible region relative to pristine $FeWO_4$. This enhancement is associated with the presence of reduced graphene oxide, which promotes extended light absorption due to its π–π^* electronic transitions and strong light-harvesting ability. Moreover, the absorption edge of the composite shows a marginal red shift toward longer wavelengths, indicating a reduction in the effective band gap energy. This shift suggests improved charge transfer interactions between $FeWO_4$ nanoparticles and rGO sheets, which facilitate electron mobility and suppress charge carrier recombination.

3.9. Fluoride (F^-) Removal Performance

Figure 9(a) compares the fluoride removal efficiency of pristine $FeWO_4$ and the $FeWO_4$/rGO nanocomposite under identical experimental conditions. As observed, $FeWO_4$ exhibits a fluoride removal efficiency of approximately 21%, indicating moderate adsorption capability toward fluoride ions. This lower performance may be attributed to the comparatively smaller surface area and limited number of active adsorption sites present on the $FeWO_4$ surface. In contrast, the $FeWO_4$/rGO nanocomposite demonstrates a significantly enhanced fluoride removal efficiency of about 33%, highlighting the positive role of rGO incorporation. The improvement in fluoride adsorption can be ascribed to the synergistic interaction between $FeWO_4$ nanoparticles and reduced graphene oxide sheets. The presence of rGO provides a larger specific surface area, increased porosity and additional functional groups, which collectively facilitate stronger electrostatic interactions and surface complexation with fluoride ions.

Furthermore, rGO acts as a supportive matrix that promotes uniform dispersion of $FeWO_4$ nanoparticles, thereby preventing particle agglomeration and exposing more active sites for adsorption. The enhanced removal efficiency observed for the $FeWO_4$/rGO composite confirms that coupling $FeWO_4$ with rGO effectively improves its adsorption performance.

a. Effect of pH on fluoride ion removal

The influence of solution pH on fluoride (F^-) removal efficiency was systematically investigated over a pH range of 3 to 12, as illustrated in the figure 9(b). The results demonstrate a strong dependence of adsorption performance on the pH of the aqueous medium.

At acidic conditions (pH 3), the fluoride removal efficiency is relatively low (12%), which can be attributed to the competition between excess hydrogen ions (H^+) and fluoride ions for the available active adsorption sites. Additionally, under highly acidic environments, partial protonation of the adsorbent surface may reduce its affinity toward fluoride ions.

As the pH increases from 3 to 7, a gradual improvement in removal efficiency is observed, reaching approximately 23% at neutral pH. This trend suggests reduced competition from protons and improved interaction between fluoride ions and the active adsorption sites of the adsorbent.The surface charge of the material becomes more favorable for adsorption in this pH range.A

significant increase in fluoride removal is observed when the pH is further raised to alkaline conditions. At pH 8, the removal efficiency sharply rises to about 40%, indicating optimal adsorption conditions. This enhanced performance may be associated with improved electrostatic attraction and possible ion-exchange mechanisms between fluoride ions and surface functional groups.

The maximum removal efficiency (42%) is achieved at pH 10, suggesting that moderately alkaline conditions are most favorable for fluoride adsorption. However, a slight decrease in removal efficiency is noted at pH 12 (39%), which can be attributed to the increased presence of hydroxide ions (OH^-). These ions compete with fluoride ions for the available adsorption sites, leading to a decrease in overall removal efficiency.

b. Effect of Catalyst Loading on Fluoride Removal

Figure 9(c) illustrates the influence of catalyst dosage on fluoride (F^-) removal efficiency using the $FeWO_4$/rGO nanocomposite. The catalyst loading was varied from 10 to 30 mg while keeping other experimental parameters constant. As shown in the figure 8(c), fluoride removal efficiency increases progressively with increasing catalyst dosage up to an optimal level.

At a catalyst dosage of 10 mg, the fluoride removal efficiency was relatively low (13%), likely due to the limited number of available active adsorption sites.As the dosage increases to 12, 14 and 16 mg, the removal efficiency improves significantly to 9%, 25% and 31%, respectively. This enhancement is primarily due to the increased surface area and higher number of active sites available for fluoride adsorption.

Further increasing the catalyst loading to 18 and 20 mg results in a marked rise in fluoride removal, reaching 37% and 42% respectively. The maximum removal efficiency of approximately 44% is observed at a catalyst loading of 25 mg, indicating the optimal dosage for fluoride adsorption under the studied conditions. The slight decrease in fluoride removal efficiency (42%) is observed when the catalyst loading is increased to 30 mg. This decrease may be due to particle agglomeration at higher dosages, which lowers the effective surface area and restricts access to adsorption sites. Furthermore, excessive catalyst loading may result in overlapping of active sites, thereby reducing adsorption efficiency.

c. Effect of Initial Fluoride Concentration on Fluoride Removal

Figure 9(d)illustrates the influence of initial fluoride (F^-) concentration on the removal efficiency of the $FeWO_4$/rGO nanocomposite under optimized experimental conditions. The initial fluoride concentration was varied in the range of 2–20 mg L^{-1}, while other parameters such as contact time, pH, and catalyst dosage were maintained constant.

As shown in the figure, the fluoride removal efficiency is highest at the lowest initial concentration, reaching approximately 58% at 2 mg L^{-1}. When the fluoride concentration increases to 5 mg L^{-1}, the removal efficiency decreases to about 45%, followed by a further reduction to 42% at 10 mg L^{-1}. A similar removal efficiency is observed at 15 mg L^{-1}, indicating saturation of available adsorption sites. At the highest concentration of 20 mg L^{-1}, the fluoride removal efficiency drops significantly to approximately 31%.

The decrease in removal efficiency with increasing fluoride concentration may be attributed to the limited availability of active adsorption sites on the $FeWO_4$/rGO surface. At lower fluoride concentrations, sufficient active sites are accessible, allowing efficient adsorption. However, as the fluoride concentration increases, competition among fluoride ions intensifies, leading to surface saturation and reduced removal efficiency. Additionally, higher ionic strength at elevated fluoride concentrations may hinder effective interaction between fluoride ions and adsorption sites.These results indicate that the $FeWO_4$/rGO nanocomposite exhibits higher fluoride removal efficiency at lower initial fluoride concentrations, highlighting the importance of optimizing pollutant concentration for effective defluoridation. These findings further demonstrate the potential of $FeWO_4$/rGO as an efficient adsorbent for fluoride removal from aqueous systems.

d. Effect of Temperature on Fluoride Removal

Figure 9(e) shows the effect of solution temperature on the fluoride (F^-) removal efficiency of the $FeWO_4$/rGO nanocomposite. The study was carried out in the temperature range of 15–40°C while maintaining constant pH, contact time, catalyst dosage, and initial fluoride concentration. At 15 °C, the fluoride removal efficiency was relatively low (27%), which can be attributed to reduced kinetic energy of fluoride ions and limited interaction between the adsorbent surface and the adsorbate. As the temperature increased to 25°C, the removal efficiency improved to approximately 33%, indicating enhanced mass transfer and increased accessibility of active adsorption sites.

A maximum fluoride removal efficiency of about 41% was achieved at 30°C, suggesting that moderate temperature conditions favor the adsorption process. The increased thermal energy at this temperature likely promotes faster diffusion of fluoride ions toward the $FeWO_4$/rGO surface and facilitates stronger surface interactions, resulting in improved adsorption efficiency.

However, further increasing the temperature to 40°C resulted in a noticeable decrease in fluoride removal efficiency (36%).This reduction may be associated with partial desorption of fluoride ions from the adsorbent surface or weakening of adsorption forces

at elevated temperatures, indicating that the adsorption process is predominantly exothermic in nature. These results demonstrate that temperature plays a significant role in fluoride adsorption, with 30 °C identified as the optimal temperature for maximum removal efficiency. These findings highlight the importance of operating temperature optimization to achieve effective and energy-efficient defluorination using $FeWO_4$/rGO nanocomposites.

e. Reusability and Stability of $FeWO_4$/rGO for Fluoride Removal

Figure 9(f) illustrates the reusability performance of the $FeWO_4$/rGO nanocomposite over five consecutive adsorption cycles for fluoride (F^-) removal under optimized experimental conditions. In the first cycle, the nanocomposite exhibits a fluoride removal efficiency of approximately 42%, demonstrating its effective adsorption capability. In subsequent cycles, a gradual decline in removal efficiency is observed, with values of 41%, 37%, 31% and 24% recorded for the second, third, fourth, and fifth cycles, respectively.

The slight decrease in adsorption efficiency after repeated cycles may be due to partial blockage of active sites by strongly adsorbed fluoride ions or incomplete desorption during regeneration.. As the number of cycles increases, further efficiency loss is likely caused by surface fouling, minor structural changes, or gradual loss of active functional groups responsible for fluoride binding.

Despite the gradual decrease, the $FeWO_4$/rGO nanocomposite maintained a considerable portion of its initial adsorption capacity after five cycles, demonstrating good structural stability and reusability. The presence of rGO plays a crucial role in maintaining mechanical integrity and preventing severe agglomeration of $FeWO_4$ particles during repeated adsorption–desorption processes. The reusability results demonstrate that $FeWO_4$/rGO is a reasonably stable and reusable adsorbent for fluoride removal, supporting its potential application in practical water treatment systems. Further optimization of regeneration methods could enhance long-term performance and improve adsorption durability.

f. Structural Stability and Reusability Analysis by XRD

Figure 9(g) presents the XRD patterns of the fresh $FeWO_4$/rGO nanocomposite and the material recovered after the fifth adsorption cycle. The diffraction pattern of the pristine $FeWO_4$/rGO sample exhibits well-defined and sharp peaks corresponding to the characteristic crystallographic planes of monoclinic $FeWO_4$, confirming its crystalline nature. These peaks are consistent with the standard diffraction data for $FeWO_4$, indicating successful formation of the nanocomposite.

After five consecutive fluoride adsorption–desorption cycles, the XRD pattern of the reused $FeWO_4$/rGO catalyst shows no noticeable shift in peak positions, and all major diffraction peaks remain clearly visible. This observation confirms that the crystal structure of $FeWO_4$ is well preserved even after repeated usage. The retention of peak positions indicates that no phase transformation or structural degradation occurred during the adsorption process.

However, the reused sample shows a slight decrease in peak intensity along with minor peak broadening. These changes may be attributed to fluoride ion adsorption on the surface, partial pore blockage, or slight loss of crystallinity during repeated adsorption–desorption and washing cycles.Importantly, no additional impurity peaks or secondary phases are detected, demonstrating that the material maintains its chemical and structural integrity throughout the reuse cycles.

Overall, the XRD results confirm the excellent structural stability and durability of the $FeWO_4$/rGO nanocomposite under repeated operational conditions. The preserved crystallinity after multiple cycles strongly supports its suitability for practical and long-term fluoride removal applications.

3.10. Antimicrobial Activity assay

The antibacterial activity of $FeWO_4$ and $FeWO_4$/rGO nanocomposites was evaluated against Gram-positive *Staphylococcus aureus* and Gram-negative *Escherichia coli* using the agar diffusion method. The observed zones of inhibition at varying concentrations are summarized and interpreted below. *S.aureus*, the control sample exhibited a consistent inhibition zone of 30 mm and were shown in figure 9. The $FeWO_4$ nanoparticles demonstrated moderate antibacterial activity, with inhibition zones of 14 mm at 100 µg/mL, increasing to 17 mm at 50 µg/mL and 19 mm at 10 µg/mL. This trend suggests improved antibacterial effectiveness at lower concentrations, possibly due to better dispersion and availability of active sites. In contrast, the $FeWO_4$/rGO nanocomposite displayed comparatively enhanced activity at higher concentrations, producing a zone of inhibition of 22 mm at 100 µg/mL and 20 mm at 50 µg/mL. However, a significant reduction to 10 mm was observed at 10 µg/mL. This indicates that the incorporation of reduced graphene oxide improves antibacterial performance at elevated concentrations, likely due to synergistic interactions between $FeWO_4$ and rGO, facilitating reactive oxygen species (ROS) generation and membrane disruption.

For *E. coli*, the control showed inhibition zones of 26 mm for $FeWO_4$ and 15 mm for $FeWO_4$/rGO. The $FeWO_4$ nanoparticles exhibited increasing

antibacterial activity with decreasing concentration, showing inhibition zones of 12 mm (100 µg/mL), 16 mm (50 µg/mL), and 19 mm (10 µg/mL). This behavior may be attributed to enhanced interaction between nanoparticles and bacterial cell walls at lower concentrations. On the other hand, $FeWO_4$/rGO nanocomposites showed limited activity against *E. coli*, with inhibition zones of 10 mm at 100 µg/mL and no detectable inhibition at 50 and 10 µg/mL. The reduced effectiveness against Gram-negative bacteria could be associated with the presence of an outer lipopolysaccharide membrane, which acts as a barrier and limits nanoparticle penetration. These results indicate that $FeWO_4$ exhibits comparatively better antibacterial activity against *E.coli*, while $FeWO_4$/rGO shows improved performance against *S.aureus* at higher concentrations. The variation in antibacterial efficiency between Gram-positive and Gram-negative bacteria highlights the influence of cell wall structure and nanoparticle interaction mechanisms.

Conclusion

The present work confirms that the $FeWO_4$/rGO nanocomposite is a more efficient adsorbent for fluoride removal than pristine $FeWO_4$, primarily due to its higher surface area, enhanced porosity, and synergistic interaction between $FeWO_4$ and reduced graphene oxide. The adsorption performance was significantly influenced by operational parameters, with optimal fluoride removal achieved at pH 10, a catalyst dosage of 25 mg and a temperature of 30°C. Lower initial fluoride concentrations favored higher removal efficiency, while increased concentrations led to site saturation. The nanocomposite also demonstrated good reusability and structural stability, maintaining appreciable performance over multiple cycles without significant structural changes. In addition to their adsorption performance, the materials demonstrated significant antibacterial activity against *Staphylococcus aureus* and *Escherichia coli*. $FeWO_4$ showed better antibacterial performance against *E. coli*, particularly at lower concentrations, whereas $FeWO_4$/rGO exhibited enhanced activity against *S. aureus* at higher concentrations. The variation in antibacterial activity highlights the role of material composition and bacterial cell structure in determining antimicrobial efficiency. Overall, the combined adsorption and antibacterial results indicate that $FeWO_4$/rGO is a stable and multifunctional material with promising potential for water treatment and environmental remediation applications.

References

1. Trojánek F, et al. Crystal structure and electronic properties of $FeWO_4$. *J Solid State Chem*. 2005;178:130-136. doi:10.1016/j.jssc.2004.11.002.
2. Errandonea D, et al. Wolframite-type tungstates: structural and optical properties. *Phys Rev B*. 2009;79:184104. doi:10.1103/PhysRevB.79.184104.
3. Zhang Y, et al. Transition metal tungstates for photocatalytic applications. *Appl Catal B Environ*. 2018;224:101-112. doi:10.1016/j.apcatb.2017.10.027.
4. Liu X, et al. Iron-based tungstates as multifunctional materials. *J Alloys Compd*. 2019;770:45-55. doi:10.1016/j.jallcom.2018.08.113.
5. Wang J, et al. Semiconducting properties of $FeWO_4$ nanostructures. *Mater Res Bull*. 2017;90:134-141. doi:10.1016/j.materresbull.2017.02.022.
6. Mohapatra D, et al. Fluoride adsorption using metal tungstates. *J Environ Chem Eng*. 2016;4:4580-4590. doi:10.1016/j.jece.2016.10.021.
7. Chen S, et al. Dye removal using tungstate-based nanomaterials. *Chem Eng J*. 2018;334:273-284. doi:10.1016/j.cej.2017.10.038.
8. Xu H, et al. Limitations of pristine metal oxide photocatalysts. *Catal Today*. 2015;252:38-44. doi:10.1016/j.cattod.2014.10.031.
9. Dreyer DR, et al. The chemistry of graphene oxide. *Chem Soc Rev*. 2010;39:228-240. doi:10.1039/B917103G.
10. Stankovich S, et al. Graphene-based composite materials. *Nature*. 2006;442:282-286. doi:10.1038/nature04969.
11. Zhang N, et al. Graphene-based photocatalysts. *Adv Mater*. 2014;26:608-621. doi:10.1002/adma.201303541.
12. Kamat PV. Graphene-based nanoarchitectures. *J Phys Chem Lett*. 2010;1:520-527. doi:10.1021/jz900222b.
13. Li Y, et al. Metal tungstate/graphene composites for environmental remediation. *ACS Appl Mater Interfaces*. 2017;9:29021-29030. doi:10.1021/acsami.7b09050.
14. Zhao H, et al. Enhanced photocatalytic activity of $FeWO_4$/rGO composites. *Appl Surf Sci*. 2019;487:556-565. doi:10.1016/j.apsusc.2019.05.144.
15. Kumar S, et al. Antibacterial properties of graphene–metal oxide hybrids. *Mater Sci Eng C Mater Biol Appl*. 2020;109:110598. doi:10.1016/j.msec.2020.110598.
16. Yang L, et al. Graphene-supported tungstate catalysts for dye degradation. *J Hazard Mater*. 2021;403:123490. doi:10.1016/j.jhazmat.2020.123490.
17. Liu J, et al. Charge transfer mechanisms in rGO-based composites. *Electrochim Acta*.

2018;259:677-686. doi:10.1016/j.electacta.2017.11.121.
18. Zhang Q, et al. Synergistic effects in graphene–metal oxide nanocomposites. *Nano Energy*. 2016;22:533-546. doi:10.1016/j.nanoen.2016.02.040.
19. Biesinger MC. Advanced analysis of metal oxides by XRD and surface techniques. *Appl Surf Sci*. 2022;597:153681. doi:10.1016/j.apsusc.2022.153681.
20. Zhang Y, et al. FTIR investigation of graphene-based metal oxide nanocomposites. *Spectrochim Acta A Mol Biomol Spectrosc*. 2021;249:119307. doi:10.1016/j.saa.2020.119307.
21. Zhou W, Apkarian R, Wang ZL. Fundamentals of scanning electron microscopy (SEM). In: Zhou W, Wang ZL, editors. *Scanning microscopy for nanotechnology*. New York: Springer; 2006. p. 1-40. doi:10.1007/978-0-387-27976-2_1.
22. Chatterjee S, et al. Elemental mapping of metal oxide–graphene nanocomposites. *Mater Charact*. 2021;177:111124. doi:10.1016/j.matchar.2021.111124.
23. Chowdhury I, Duch MC, Mansukhani ND, Hersam MC. Interactions of graphene oxide nanomaterials with natural organic matter and metal oxide surfaces. *Environ Sci Technol*. 2014;48(16):9382-9390. doi:10.1021/es5012579.
24. Liu J, et al. Surface area–activity relationships in graphene-based adsorbents. *Chem Eng J*. 2021;420:127694. doi:10.1016/j.cej.2020.127694.
25. Sanjay Krishna M, Balaji S, Vadamalai Raj G, Pravin PA, Sathish Kumar M, Kothurkar NK, et al. Polymer-iron tungstate-reduced graphene oxide nanocomposites for microwave absorption. *IOP Conf Ser Mater Sci Eng*. 2019;577(1):012079. doi:10.1088/1757-899X/577/1/012079.
26. Kovács TN, Pokol G, Gáber F, Nagy D, Igricz T, Lukács IE, et al. Preparation of iron tungstate ($FeWO_4$) nanosheets by hydrothermal method. *Mater Res Bull*. 2017;95:563-569. doi:10.1016/j.materresbull.2017.07.031.
27. Zaaba NI, Foo KL, Hashim U, Tan SJ, Liu WW, Voon CH. Synthesis of graphene oxide using modified Hummers method: solvent influence. *Procedia Eng*. 2017;184:469-477. doi:10.1016/j.proeng.2017.02.940.
28. Thirumoorthi G, Gnanavel B, Kalaivani M, Ragunathan A, Venkatesan H. Suitability of iron (Fe)-doped tungsten oxide (WO_3) nanomaterials for photocatalytic and antibacterial applications. *Int J Nanosci*. 2021;20(5):2150042. doi:10.1142/S0219581X21500423.
29. Ayyappan S, Nithya R, Sivaranjani T, Karthigeyan A, Rajakarthihan S, Bharath G. Enhanced photoelectrocatalytic and antibacterial performance of g-C_3N_4/$ZnWO_4$ heteronanostructures for sustainable water purification. *Ceram Int*. 2025;51(11):14565-14574. doi:10.1016/j.ceramint.2025.02.052.
30. Selvakumar P, Thiyagarajan S, Ganesan S, Calisius S. Multifunctional nickel tungstate nanoparticles: a dual approach for high-performance supercapacitors and antimicrobial applications. *Eur Phys J Plus*. 2025;140(7):651. doi:10.1140/epjp/s13360-025-06616-5.
31. Manami RB, Megalamani MB, Kalkhambkar RG, Nandibewoor ST, Adarakatti PS, Narasimharao K, et al. High-performance detection of tryptophan using a $NiWO_4$/RGO nanohybrid modified electrode in environmental applications. *Ionics*. 2026:1-21. doi:10.1007/s11581-026-05423-8.
32. Balasurya S, Alfarraj S, Raju LL, Chinnathambi A, Alharbi SA, Thomas AM, et al. Novel $CoWO_4$-Ag_2MoO_4 NCs: synthesis, enhanced photocatalytic activity under visible-light irradiation and its antimicrobial activity. *Surf Interfaces*. 2021;25:101237. doi:10.1016/j.surfin.2021.101237.
33. Goda MN, Alqarni LS, Khairy M, Abou-Krisha MM, Abdulkhair BY, Abdelrahman EA, et al. Hydrothermal synthesis of microporous $CuWO_4$ for hydrogen generation and antibacterial activity. *J Inorg Organomet Polym Mater*. 2025;35(9):7218-7232. doi:10.1007/s10904-025-03611-6.
34. Manami RB, Megalamani MB, Kalkhambkar RG, Adarakatti PS, Nandibewoor ST, Narasimharao K, et al. Advancement in highly selective electrochemical sensing of Pb(II) using $CuWO_4$/RGO nanocomposite modified electrode. *J Mater Sci Mater Electron*. 2025;36(36):2268. doi:10.1007/s10854-025-14125-9.
35. Kundu S, Ma L, Chen Y, Liang H. Microwave assisted swift synthesis of $ZnWO_4$ nanomaterials: material for enhanced photo-catalytic activity. *J Photochem Photobiol A Chem*. 2017;346:249-264. doi:10.1016/j.jphotochem.2017.06.012.

Table 1: Extended Comparative Performance of $FeWO_4$ and $FeWO_4$/ rGO Nanocomposites

Material	Synthesis Method	Fluoride Removal (%)	Antibacterial Activity (mm)	Key Observation	Reference
$FeWO_4$	Sol–gel	21	14–19 (*S. aureus*)	Moderate performance	28
$ZnWO_4$	Precipitation	25	12–18 (*S. aureus*)	Stable photocatalyst	29
$NiWO_4$	Sol–gel	28	10–16 (*E. coli*)	Moderate antibacterial effect	30
$NiWO_4$/rGO	Hydrothermal	38	20–24 (*S. aureus*)	High multifunctionality	31
$CoWO_4$	Hydrothermal	24	12–16 (*S. aureus*)	Limited charge separation	32
$CuWO_4$	Sol–gel	26	10–15 (*E. coli*)	Narrow bandgap catalyst	33
$CuWO_4$/rGO	Hydrothermal	37	18–22 (*S. aureus*)	Improved electron transfer	34
$MnWO_4$	Precipitation	23	11–16 (*S. aureus*)	Moderate catalytic activity	35
$FeWO_4$/rGO	Hydrothermal	40	20–22 (*S. aureus*)	Strong synergistic effect	In this study

Table 2 : Antibacterial activity of the $FeWO_4$ and $FeWO_4$/rGO nanocomposite

Test micro-organism	Anti-bacterial activity			
	$FeWO_4$		$FeWO_4$/rGO	
	Concentration (µg/mL)	Zone of Inhibition (mm)	Concentration (µg/mL)	Zone of Inhibition (mm)
S.Aureus	Control	30	Control	30
	100	14	100	22
	50	17	50	20
	10	19	10	10
E.coli	Control	26	Control	15
	100	12	100	10
	50	16	50	0
	10	19	10	0

Figures

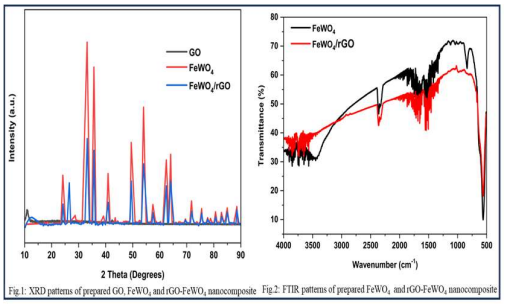

Fig.1: XRD patterns of prepared GO, $FeWO_4$ and rGO-$FeWO_4$ nanocomposite Fig.2: FTIR patterns of prepared $FeWO_4$ and rGO-$FeWO_4$ nanocomposite

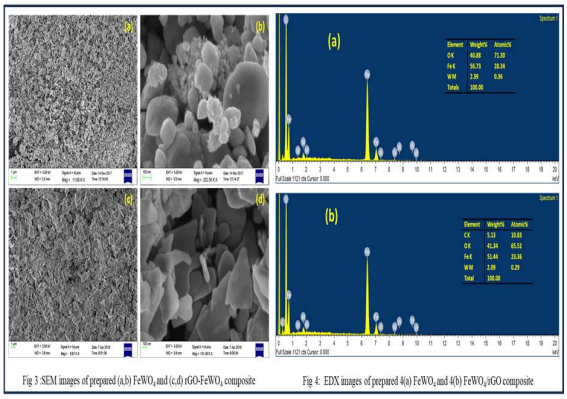

Fig 3: SEM images of prepared (a,b) $FeWO_4$ and (c,d) rGO-$FeWO_4$ composite Fig 4: EDX images of prepared 4(a) $FeWO_4$ and 4(b) $FeWO_4$/rGO composite

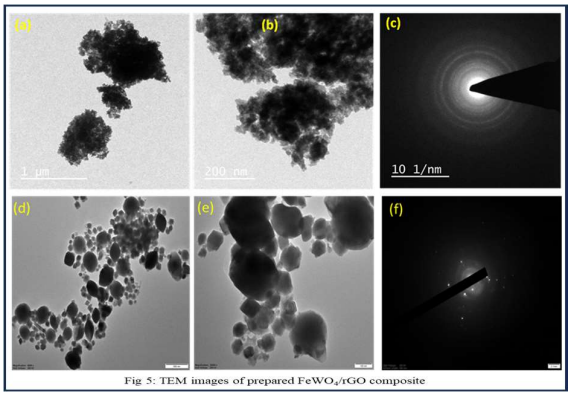

Fig 5: TEM images of prepared $FeWO_4$/rGO composite

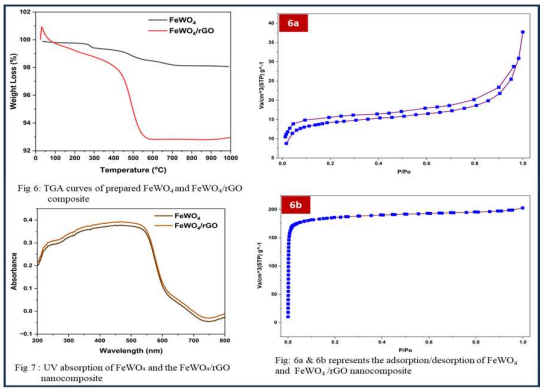

Fig 6: TGA curves of prepared $FeWO_4$ and $FeWO_4$/rGO composite

Fig 7 : UV absorption of $FeWO_4$ and the $FeWO_4$/rGO nanocomposite

Fig: 6a & 6b represents the adsorption/desorption of $FeWO_4$ and $FeWO_4$ /rGO nanocomposite

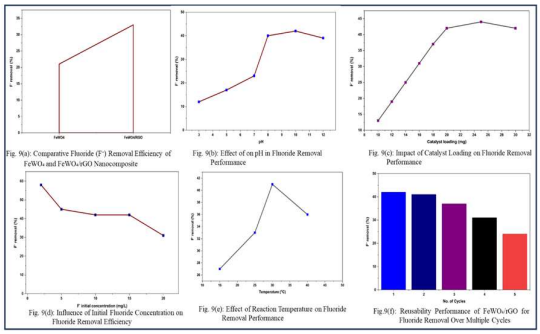

Fig. 9(a): Comparitive Fluoride (F⁻) Removal Efficiency of $FeWO_4$ and $FeWO_4$/rGO Nanocomposite

Fig. 9(b): Effect of on pH in Fluoride Removal Performance

Fig. 9(c): Impact of Catalyst Loading on Fluoride Removal Performance

Fig. 9(d): Influence of Initial Fluoride Concentration on Fluoride Removal Efficiency

Fig. 9(e): Effect of Reaction Temperature on Fluoride Removal Performance

Fig.9(f): Reusability Performance of $FeWO_4$/rGO for Fluoride Removal Over Multiple Cycles

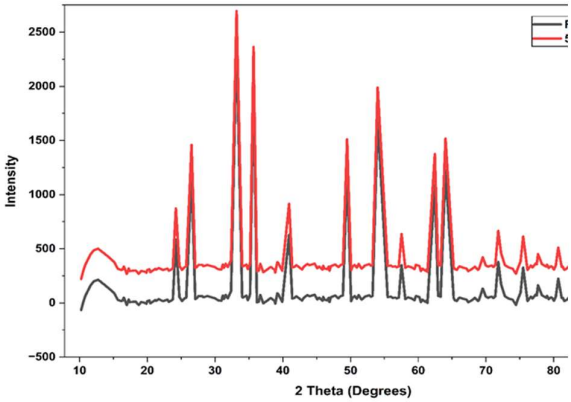

Fig. 10: Analysis of Structural Stability and Reusability Usir Patterns

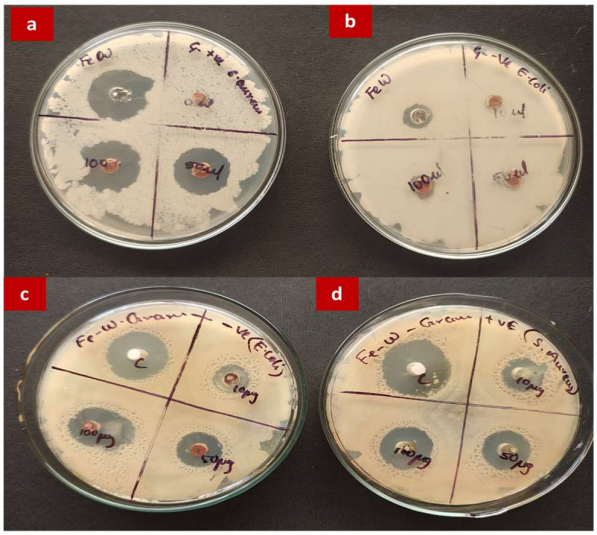

Fig 11: Anti-bacterial activity of $FeWO_4$ (a,b)and $FeWO_4$/rGO (c,d) against *S.Aureus* and *E.Coli*